Spinodal phase separation in relativistic nuclear collisions

Jørgen Randrup
Nuclear Science Division, Lawrence Berkeley National Laboratory, Berkeley, California 94720, USA
(Received 1 July 2010; published 7 September 2010)

The spinodal amplification of density fluctuations is treated perturbatively within dissipative fluid dynamics for the purpose of elucidating the prospects for this mechanism to cause a phase separation to occur during a relativistic nuclear collision. The present study includes not only viscosity but also heat conduction (whose effect on the growth rates is of comparable magnitude but opposite), as well as a gradient term in the local pressure, and the corresponding dispersion relation for collective modes in bulk matter is derived from relativistic fluid dynamics. A suitable two-phase equation of state is obtained by interpolation between a hadronic gas and a quark-gluon plasma, while the transport coefficients are approximated by simple parametrizations that are suitable at any degree of net baryon density. We calculate the degree of spinodal amplification occurring along specific dynamical phase trajectories characteristic of nuclear collision at various energies. The results bring out the important fact that the prospects for spinodal phase separation to occur can be greatly enhanced by careful tuning of the collision energy to ensure that the thermodynamic conditions associated with the maximum compression lie inside the region of spinodal instability.

DOI: 10.1103/PhysRevC.82.034902 PACS number(s): 25.75.−q, 81.30.Dz, 64.75.Gh, 64.60.an

I. INTRODUCTION

It is expected that the confined and deconfined phases of strongly interacting matter may coexist at net baryon densities above a certain critical value, and significant experimental efforts are underway to search for evidence of the associated first-order phase transition and its critical end point: A systematic beam-energy scan is currently being performed at the Relativistic Heavy Ion Collider (RHIC) at BNL to look for the critical point [1]; the CBM experiment at the Facility for Antiproton and Ion Research (FAIR) at GSI will study baryon-dense matter and search for the phase transition [2]; and the proposed Nuclotron-based Ion Collider Facility (NICA) at JINR aims at exploring the mixed phase [3].

These studies are rather challenging, not only because it is inherently difficult to extract the properties of equilibrium bulk matter from collision experiments, but also because there is currently no suitable transport model available for guiding these efforts. As a result, there is currently an urgent need for identifying experimentally observable signals of the phase structure.

The present paper focuses on the possibility that the mechanism of spinodal phase decomposition may have effects that could be exploited as signals of the phase transition. Spinodal decomposition is a well-known generic phenomenon associated with first-order phase transitions that has been studied in a variety of substances and also found industrial application [4]. Furthermore, nuclear spinodal fragmentation [5] was observed in nuclear collisions at intermediate energies [6] several years ago. A preliminary study [7] found grounds for guarded optimism that spinodal separation between the confined and deconfined phases could in fact occur in relativistic collisions and we have therefore undertaken the present more refined analysis.

While that earlier study [7] employed a somewhat schematic equation of state based on a generalized classical gas, the present uses a more realistic equation of state obtained by interpolating between a hadron gas and a quark-gluon plasma. An advantage of this procedure is that it automatically incorporates the increase in the number of degrees of freedom in the dense (deconfined) phase, a peculiar but important characteristic of strongly interacting matter. Building on the developments in Ref. [7], we take account of finite-range effects by including a gradient term in the equation of state. This refinement is essential for obtaining a physically meaningful description because it ensures both that there is an interface tension between the two coexisting phases and that the spinodal growth rates subside at large wave numbers.

We again carry out our studies within the framework of fluid dynamics, because this type of transport description has the distinct advantage that the complicated and still poorly understood microstructure of the system enters only via the equation of state and the transport coefficients. A general discussion of the fluid-dynamical description of first-order phase transitions was given recently in Ref. [8].

Although the dispersion equation in [7] was derived with both shear and bulk viscosity included, the actual calculations were done for ideal fluid dynamics. In the present study, the dynamical calculations include not only viscosity but also heat conductivity, which proves to be as important as viscosity while affecting the spinodal growth rates oppositely, as we demonstrate quantitatively. The associated cubic dispersion equation is derived directly from relativistic fluid dynamics. The medium dependence of the transport coefficients is expressed in terms of the local values of the enthalpy density and the particle spacing, an approximation that applies not only in the baryon-poor regime but also in the baryon-dense media of relevance to the phase transition. The strength of the transport coefficients for arbitrary density and temperature can thus be related to the values obtained from analyses of the RHIC data.

We seek to construct plausible dynamical phase trajectories by invoking results from earlier calculations with various

transport models, and we examine in particular the crucial importance of using a collision energy for which the maximum compression occurs inside the spinodal phase region. Once the phase trajectory of the collision system has been specified, we may integrate the spinodal growth rate along the dynamical history and thus calculate the resulting degree of amplification as a function of the wave number of the density perturbation. We do that for a range of dissipation strengths that bracket those expected from the analysis of the RHIC data.

The present, more refined, studies suggest that spinodal phase decomposition may indeed be triggered during nuclear collisions within a certain (likely relatively narrow) optimal energy range. This expectation is rather insensitive to the still poorly known strength of the transport coefficients. Such a spinodal phase separation would result in an assembly of plasma drops embedded in a hadron gas, and our present analysis permits us to estimate the typical drop size.

There is some similarity between the spinodal instabilities studied here, for which the baryon density plays the role of the order parameter, and those associated with the chiral order parameter. (Dynamical studies of this latter mechanism in expanding matter have been carried out within the linear σ model both with [9] and without [10] explicit quark degrees of freedom.) However, the associated dispersion relations differ qualitatively in the limit of long wave lengths: Whereas the growth rate for the unstable pion modes tend to a constant, the density instabilities grow in proportion to the wave number, as occurs in fluid dynamics.

The presentation is organized as follows. We first discuss the expected thermodynamic phase structure of strongly interacting matter within the framework of the specific equation of state that we have constructed. We then turn to dissipative fluid dynamics within which we derive the dispersion equation for the collective modes in bulk matter. Subsequently we develop expressions for the transport coefficients in baryon-rich matter and use those in calculations of the spinodal growth rates. Finally, we obtain quantitative results for the degree of spinodal amplification experienced by the bulk of the collision system as it evolves along various plausible phase trajectories. The construction of the equation of state and the associated spline procedure are described in appendices.

II. THERMODYNAMIC PHASE STRUCTURE

To make quantitative studies, we need to employ a specific equation of state that is plausibly realistic and, in particular, exhibits the expected phase structure.

Although significant progress has been made in understanding the thermodynamic properties of the confined and deconfined phases separately, our current understanding of the phase coexistence region is not yet on firm ground. We therefore employ a conceptually simple approximate equation of state in which the region of phase transformation is described by means of a suitable interpolation between an idealized hadron gas and an idealized quark-gluon plasma. The details of this construction are described in Appendix A, while the resulting phase structure is shown in Fig. 1.

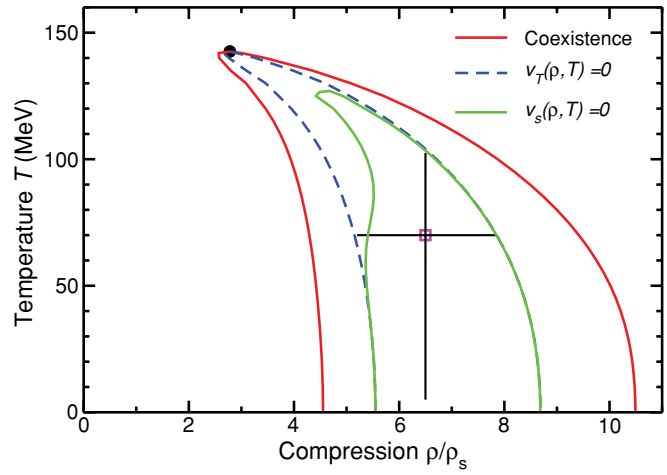

FIG. 1. (Color online) The (ρ, T) phase diagram for bulk matter showing the phase coexistence boundary (outer solid), the isothermal spinodal where $v_T = 0$ (dashed), and the isentropic spinodal where $v_s = 0$ (inner solid), together with the critical point (for details, see Appendix A). The dispersion relation shown in Fig. 2 was calculated at the square and the results shown in Fig. 3 were obtained along the two straight lines.

For the present study, it is convenient to work in the canonical representation where the thermodynamic state of the system is characterized by the temperature T and the (net) baryon density $\rho = n_B - n_{\bar{B}}$. (In the phase region of primary interest, the temperature is relatively low and the chemical potential relatively high, so the equilibrium population of antibaryons is relatively insignificant, $n_{\bar{B}} \ll n_B$.) The key thermodynamic function is then the free-energy density, s $f_T(\rho)$, from which the other quantities may be obtained,

$$\text{Chemical potential}: \quad \mu_T(\rho) = \partial_\rho f_T(\rho), \tag{1}$$

$$\text{Pressure}: \quad p_T(\rho) = \rho\partial_\rho f_T(\rho) - f_T(\rho), \tag{2}$$

$$\text{Entropydensity}: \quad \sigma_T(\rho) = -\partial_T f_T(\rho), \tag{3}$$

$$\text{Energydensity}: \quad \varepsilon_T(\rho) = f_T(\rho) - T\partial_T f_T(\rho) \tag{4}$$

We may also express the isothermal sound speed v_T,

$$v_T^2 \equiv \frac{\rho}{h_T}\left(\frac{\partial p}{\partial \rho}\right)_T = \frac{\rho}{h_T}\partial_\rho p_T(\rho) = \frac{\rho^2}{h_T}\partial_\rho^2 f_T(\rho), \tag{5}$$

where $h_T(\rho) = p_T(\rho) + \varepsilon_T(\rho)$ is the enthalpy density, as well as the isentropic sound speed v_s,

$$v_s^2 \equiv \frac{\rho}{h_T}\left(\frac{\partial p}{\partial \rho}\right)_s = v_T^2 + \frac{T}{h_T}\frac{1}{c_v}(\partial_T p_T(\rho))^2 \geqslant v_T^2, \tag{6}$$

where the specific heat is $c_v \equiv \partial_T \varepsilon_T(\rho) = T\partial_T \sigma_T(\rho)$.

Different manifestations of the system that have the same values of temperature, chemical potential, and pressure are in mutual thermodynamic equilibrium and may thus coexist. As Fig. 1 shows, such phase coexistence occurs for temperatures below the critical value, $T < T_c \approx 142.5$ MeV. The corresponding density values, ρ_1^T and ρ_2^T, are traced out (outer solid curve). Inside this boundary, it is thermodynamically favorable for uniform matter to separate into the two coexisting phases. However, in the part of the phase coexistence region that is close to the boundary, small deviations from uniformity

are thermodynamically unfavorable and here the system is mechanically metastable, as signalled by the fact that $v_T^2 > 0$ in this phase region. Furthermore, finite fluctuations of sufficient magnitude may act as nucleation seeds that are amplified into droplets or bubbles (in the low- or high-density metastable region, respectively), a phenomenon that has been studied for strongly interacting matter at low or vanishing density [11].

The situation changes radically at the spinodal boundary where the isothermal sound speed vanishes, $v_T = 0$ (the dashed curve in Fig. 1): Inside this boundary even infinitesimal deviations from uniformity are thermodynamically favorable and bulk matter is thus mechanically unstable. As a consequence, small density fluctuations may be amplified and thereby cause the system to undergo a spontaneous phase separation. The phase region of spinodal instability extends in temperature all the way from zero up to T_c.

Finally, Fig. 1 also shows the boundary where the isentropic sound speed vanishes, $v_s = 0$. Inside this smaller phase region, the spinodal amplification process can occur without any entropy production. This special region does not extend all the way up to T_c and it narrows considerably as the temperature approaches its upper bound.

The equation of state applies to idealized uniform matter. However, since we are interested in following the evolution of density disturbances, it is essential to include finite-range effects. Indeed, the physical coexistence between two different phases along a common interface could not be realized without taking proper account of the density gradients, nor could the associated interface tension be obtained. We shall therefore augment the bulk thermodynamics with a gradient term as proposed in Ref. [7] (see Sec. III C 1), which then extends the validity of the equation of state to nonuniform systems. In particular, it is possible to describe the diffuse interface between two coexisting phases and the associated tension. Furthermore, as we shall see, the gradient term is essential for obtaining a physically reasonable dispersion relation because it stabilizes disturbances having a small spatial scale.

III. DISSIPATIVE FLUID DYNAMICS

We wish to employ dissipative fluid dynamics for our dynamical studies. Fluid dynamics is convenient because the specific microscopic structure of the matter under consideration enters only via the equation of state and a few transport coefficients. On the other hand, the treatment relies on the assumption of approximate local equilibrium which may generally be questionable in nuclear collisions. Fortunately, our applications are to collisions of relatively modest energies and, moreover, to the later stages in the evolution. Thus, the conditions for applicability should be reasonably favorable.

We base our treatment on the relativistic formulation by Muronga [12]. The four-velocity of the local flow is $u^\mu = (\gamma, \gamma \boldsymbol{v})$ and the symmetric tensor $\Delta^{\mu\nu} \equiv g^{\mu\nu} - u^\mu u^\nu$ projects onto the three-space orthogonal to u^μ, $\Delta^{\mu\nu} u_\nu = 0$.

The space-time derivative decomposes, $\partial^\mu = u^\mu D + \nabla^\mu$, where the convective time derivative is $D \equiv u^\mu \partial_\mu = \gamma[\partial_t + \boldsymbol{v} \cdot \boldsymbol{\nabla}]$ while the gradient is $\nabla^\mu \equiv \Delta^{\mu\nu}\partial_\nu$.

The equations of motion simplify when expressed in a specific reference frame. For the present study, it is convenient to use the Eckart frame, which is defined in terms of the charge flow and is usually employed in nonrelativistic scenarios. Then, because the local charge flow, V^μ, vanishes by definition, the charge four-current density is $N^\mu = \rho u^\mu$, where ρ is the charge density in the local flow frame. (However, it may generally be preferable to use the Landau frame because it is defined in terms of the energy flow and is thus meaningful also for chargeless fluids and fluids with several conserved charges for which there is no unique generalization of the Eckart frame.)

A. Small disturbances

We consider the early evolution of small deviations from uniformity. We generally assume that these are planar and harmonic, $\rho(\boldsymbol{r}, t) = \rho_0 + \rho_k \exp(ikx - i\omega t)$ with $\delta \equiv |\rho_k|/\rho_0 \ll 1$, and similarly for the other quantities. We may then ignore terms of order $\mathcal{O}(\delta^2)$ and higher. It follows that the associated flow velocities are small, $v \ll 1$ because $\mathcal{O}(v) = \mathcal{O}(\delta)$, and thus we have $\gamma \equiv [1 - v^2]^{-1/2} = 1 + \mathcal{O}(\delta^2) \approx 1$.

Generally, the energy flow is given by $W^\mu \equiv q^\mu + hV^\mu = q^\mu$, where q^μ is the heat flow and $h = p + \varepsilon$ the enthalpy density. Because the local charge flow V^μ vanishes when we use the Eckart frame (see above text), the energy flow equals the heat flow, $W^\mu = q^\mu$, and is $\mathcal{O}(\delta)$. Hence, $\mathcal{O}(Wu) = \mathcal{O}(\delta^2)$, and the energy-momentum tensor simplifies to

$$T^{\mu\nu} = \varepsilon u^\mu u^\nu - p\Delta^{\mu\nu} + \pi^{\mu\nu} - \Pi\Delta^{\mu\nu}. \tag{7}$$

Here, $\varepsilon = u_\mu T^{\mu\nu} u_\nu$ is the energy density in the local flow frame and $p + \Pi = -\frac{1}{3}\Delta_{\mu\nu} T^{\mu\nu}$ is the sum of the local isotropic pressure p and the pressure induced by the bulk viscosity which enters through the bulk pressure,

$$\Pi = -\zeta \nabla_\mu u^\mu \approx -\zeta \nabla_i v^i = -\zeta \partial_i v^i = -\zeta \boldsymbol{\nabla} \cdot \boldsymbol{v}. \tag{8}$$

Furthermore, the heat flow is $q^\mu = u_\nu T^{\nu\lambda} \Delta^\mu_\lambda$, while the shear viscosity enters via the stress tensor,

$$\pi^{\mu\nu} = \eta\big[\Delta^\mu_\sigma \Delta^\nu_\tau + \Delta^\mu_\tau \Delta^\nu_\sigma - \tfrac{2}{3}\Delta^{\mu\nu}\Delta_{\sigma\tau}\big]\nabla^\sigma u^\tau \tag{9}$$

$$\approx \eta\big[\Delta^\mu_i \Delta^\nu_j + \Delta^\mu_j \Delta^\nu_i - \tfrac{2}{3}\Delta^{\mu\nu}\Delta_{ij}\big]\nabla^i v^j, \tag{10}$$

where we have used that only the spatial components of ∇^σ contribute to leading order in δ and, moreover, any derivatives of $u^0 \approx 1$ can be ignored so only the spatial components $u^i \approx v^i$ contribute. Furthermore, because $\Delta^0_i = v^i$, which is $\mathcal{O}(\delta)$, only the spatial elements $\Delta^i_j \approx \delta_{ij}$ contribute. Hence, only the 3×3 spatial part $\boldsymbol{\pi}$ is nonvanishing. It has the following elements,

$$\pi^{ij} \approx -\eta\big[\partial_i v^j + \partial_j v^i - \tfrac{2}{3}\delta_{ij}\partial_k v^k\big]. \tag{11}$$

Thus, for small deviations from uniformity, the spatial part $\boldsymbol{T}$ of the energy-momentum tensor is given by

$$T^{ij} \approx \delta_{ij} p - \eta\big[\partial_i v^j + \partial_j v^i - \tfrac{2}{3}\delta_{ij}\partial^k v^k\big] - \zeta\delta_{ij}\boldsymbol{\nabla}\cdot\boldsymbol{v}. \tag{12}$$

If the spatial variation of the viscosity coefficients η (shear) and ζ (bulk) may be ignored, we have

$$\boldsymbol{\nabla}\cdot\boldsymbol{T} \approx \boldsymbol{\nabla} p - \eta\boldsymbol{\Delta}\boldsymbol{v} - \big[\tfrac{1}{3}\eta + \zeta\big]\boldsymbol{\nabla}(\boldsymbol{\nabla}\cdot\boldsymbol{v}). \tag{13}$$

The gradient simplifies further in a semi-infinite geometry (where the only spatial variation is in the x direction),

$$\boldsymbol{\nabla}\cdot\boldsymbol{T} \asymp \partial_x T_{xx} \approx \partial_x p - \left[\tfrac{4}{3}\eta+\zeta\right]\partial_x^2 v. \tag{14}$$

Thus, only the *effective* viscosity $\xi \equiv \frac{4}{3}\eta+\zeta$ enters. It follows that a uniform stretching, $v(x)\sim x$, is dissipation free. We also wish to point out that the shear viscosity contributes even though the flow has no shear.

It is interesting to note that the above result reflects a general feature of isotropic expansions in N dimensions. To see this, assume that $\rho(\boldsymbol{r})=\rho(r)$ and $\boldsymbol{v}(\boldsymbol{r})=v(r)\hat{\boldsymbol{r}}$. The viscous term in the Euler equation may then be evaluated by use of spherical coordinates,

$$\eta\boldsymbol{\Delta v}+\left[\frac{1}{3}\eta+\zeta\right]\boldsymbol{\nabla}(\boldsymbol{\nabla}\cdot\boldsymbol{v}) = \xi\,\hat{\boldsymbol{r}}\,\partial_r\frac{1}{r^{N-1}}\partial_r r^{N-1}v. \tag{15}$$

Thus, it is always the combination $\xi\equiv\frac{4}{3}\eta+\zeta$ that enters. Furthermore, it follows that a Hubble-type expansion, $v(r)\sim r$, is dissipation free in any dimension.

B. Equations of motion

The fluid-dynamic equations of motion reflect the conservation of (baryon) charge, momentum, and energy. We are interested in the dynamics of small deviations from uniformity in a semi-infinite configuration and we focus on harmonic disturbances,

$$\rho(\boldsymbol{r},t)=\rho_0+\delta\rho(x,t) \doteq \rho_0+\rho_k\,e^{ikx-i\omega t}, \tag{16}$$

$$\varepsilon(\boldsymbol{r},t)=\varepsilon_0+\delta\varepsilon(x,t) \doteq \varepsilon_0+\varepsilon_k\,e^{ikx-i\omega t}, \tag{17}$$

$$p(\boldsymbol{r},t)=p_0+\delta p(x,t) \doteq p_0+p_k\,e^{ikx-i\omega t}, \tag{18}$$

and similarly for the other dynamical variables.

The conservation of charge is ensured by the continuity equation, $\partial_\mu N^\mu \doteq 0$, which here becomes

$$C:\ \partial_t\rho \doteq -\rho_0\partial_x v \ \Rightarrow\ \omega\rho_k \doteq \rho_0 k v_k. \tag{19}$$

It serves to eliminate the flow velocity, $v_k=\omega\rho_k/(\rho_0 k)$. The momentum equation simplifies considerably for the present scenario of small disturbances,

$$M:\ h_0\partial_t v \doteq -\partial_x[p-\zeta\,\partial_x v]-\partial_x\pi_{xx}-\partial_t q, \tag{20}$$

where $h_0=p_0+\varepsilon_0$ is the enthalpy density of the uniform system and the heat flow is $\boldsymbol{q}=(q,0,0)$ (see below). The equation for energy conservation is similarly simplified,

$$E:\ \partial_t\varepsilon \doteq -h_0\partial_x v-\partial_x q. \tag{21}$$

By combining these latter two equations, (20) and (21), one obtains the sound equation,

$$\partial_t E-\partial_x M:\ \partial_t^2\varepsilon \doteq \partial_x^2\Delta[p-\zeta\,\partial_x v]+\partial_x^2\pi_{xx}, \tag{22}$$

which amounts to $\omega^2\varepsilon_k \doteq k^2 p_k - i\xi(\omega/\rho_0)k^2\rho_k$ where we recall that $\xi\equiv\frac{4}{3}\eta+\zeta$ [see Eq. (14)].

C. Dispersion equation

When heat conductivity is ignored ($\kappa=0$), the energy density tracks the charge density, as follows immediately from the energy equation, $\rho_0\varepsilon_k \doteq h_0\rho_k$. Furthermore, in the absence of a gradient term in the equation of state (see later), we have $p_k=p_\varepsilon\varepsilon_k+p_\rho\rho_k$ with $p_\varepsilon\equiv\partial_\varepsilon p_0(\varepsilon,\rho)$ and $p_\rho\equiv\partial_\rho p_0(\varepsilon,\rho)$ where $p_0(\varepsilon,\rho)$ is the microcanonical equation of state. Since the isentropic sound speed v_s is given by $v_s^2=p_\varepsilon+(\rho_0/h_0)p_\rho$, we obtain the familiar viscous dispersion equation, $\omega^2=v_s^2k^2-i\xi(\omega/h_0)k^2$ [7].

To obtain the dispersion equation with heat conductivity included, we must invoke the form of the heat current,

$$q\approx-\kappa[\partial_x T+T_0\partial_t v]:\ q_k=-i\kappa\left[kT_k-\frac{T_0}{\rho_0}\frac{\omega^2}{k}\rho_k\right]. \tag{23}$$

Insertion of this expression into the energy equation (21) yields a relationship between ρ_k, ε_k, and T_k,

$$\varepsilon_k = \frac{h_0}{\rho_0}\rho_k+\frac{k}{\omega}q_k \approx \frac{h_0}{\rho_0}\rho_k-i\kappa\frac{k^2}{\omega}T_k, \tag{24}$$

where the term $\sim\kappa\rho_k$ has been ignored because if is $\mathcal{O}(\kappa)$ in comparison with $(h_0/\rho_0)\rho_k$. Thermodynamics enables us to express $\delta\varepsilon$ in terms of δT and $\delta\rho$,

$$\varepsilon_k=\left(\frac{\partial\varepsilon}{\partial T}\right)_\rho T_k+\left(\frac{\partial\varepsilon}{\partial\rho}\right)_T\rho_k = c_v T_k-\frac{\sigma_{\varepsilon\rho}}{\sigma_{\varepsilon\varepsilon}}\rho_k, \tag{25}$$

where $\sigma_{\varepsilon\varepsilon}\equiv\partial_\varepsilon^2\sigma_0(\varepsilon,\rho)$ and $\sigma_{\varepsilon\rho}\equiv\partial_\varepsilon\partial_\rho\sigma_0(\varepsilon,\rho)$ are second derivatives of the entropy density $\sigma_0(\varepsilon,\rho)$. We have also used $(\partial\varepsilon/\partial T)_\rho=c_v=-1/T\sigma_{\varepsilon\varepsilon}$, the heat capacity at constant density. Using, furthermore,

$$h_0\sigma_{\varepsilon\varepsilon}+\rho_0\sigma_{\rho\varepsilon} = -\left(\frac{\partial p}{\partial\varepsilon}\right)_\rho, \tag{26}$$

we may then obtain T_k from the energy equation (21),

$$T_k \approx \frac{1}{1+i\kappa k^2/\omega c_v}\frac{T_0}{\rho_0}\left(\frac{\partial p}{\partial\varepsilon}\right)_\rho\rho_k. \tag{27}$$

The canonical equation of state $p_T(\rho)$ allows us to express the pressure variation in terms of the variations in temperature and density,

$$p_k=\left(\frac{\partial p}{\partial T}\right)_\rho T_k+\left(\frac{\partial p}{\partial\rho}\right)_T\rho_k=\left(\frac{\partial p}{\partial\varepsilon}\right)_\rho c_v T_k+\frac{h_0}{\rho_0}v_T^2\,\rho_k, \tag{28}$$

where v_T is the isothermal sound speed [see Eq. (5)].

With these preparations, the dispersion equation can then be obtained by substituting the relations (25), (27), and (28) into the sound equation and using the relationship $v_s^2-v_T^2=(T/h)(\partial p/\partial T)_\rho(\partial p/\partial\varepsilon)_\rho$,

$$\omega^2 \doteq v_T^2k^2-i\xi\frac{\omega}{h_0}k^2+\frac{v_s^2-v_T^2}{1+i\kappa k^2/\omega c_v}k^2, \tag{29}$$

retaining heat conduction terms only up to $\mathcal{O}(\kappa)$. This is recognized as the dispersion equation given in Ref. [13].

1. *Gradient correction*

As noted above (end of Sec. II), it is essential to take account of finite-range effects, without which the spinodal growth rate

would become ever larger as the wave number is increased [14]. Following Ref. [7], we introduce a gradient correction in the equation of state. To leading order in the disturbance amplitudes, the effect of the gradient term on the local pressure is given by

$$p(\boldsymbol{r}) \;\approx\; p_0(\varepsilon(\boldsymbol{r}), \rho(\boldsymbol{r})) - C\rho_0\nabla^2\rho(\boldsymbol{r}), \tag{30}$$

where $p_0(\varepsilon, \rho)$ is the microcanonical equation of state, (i.e., the pressure in uniform matter having the specified energy and charge densities). The pressure amplitude is then modified accordingly,

$$p_k \rightsquigarrow p_k + C\rho_0 k^2 \rho_k. \tag{31}$$

Hence, we should augment the ρ_k term in Eq. (28),

$$\frac{h_0}{\rho_0} v_T^2 \rho_k \rightsquigarrow \left[\frac{h_0}{\rho_0} v_T^2 + C\rho_0 k^2\right] \rho_k. \tag{32}$$

The full dispersion equation is then

$$\omega^2 \;\doteq\; v_T^2 k^2 + C\frac{\rho_0^2}{h_0}k^4 - i\xi\frac{\omega}{h_0}k^2 + \frac{v_s^2 - v_T^2}{1 + i\kappa k^2/\omega c_v}k^2, \tag{33}$$

that is, the gradient term $\sim Ck^4$ is simply added, just as when there is no heat conductivity [7].

2. *Solution of the dispersion equation*

When heat conductivity is included, $\kappa > 0$, the dispersion equation is of third order and, consequently, there are three eigenvalues for each wave vector $\boldsymbol{k}$, as one would generally expect since the energy density ε is now no longer tied to the baryon density ρ. This equation has one purely imaginary solution, $\omega_{\boldsymbol{k}}^0 = i\gamma_k^0$, and a pair of generally complex solutions, $\omega_{\boldsymbol{k}}^{\pm}$, which are either both also imaginary, $\omega_{\boldsymbol{k}}^{\pm} = i\gamma_k^{\pm}$, or have the form $\omega_{\boldsymbol{k}}^{\pm} = \mp\epsilon_k + i\gamma_k$. In the latter case it is easy to see that $\gamma_k < 0$ in the normal region where $v_T^2 > 0$.

The two frequencies $\mathring{\omega}_k^{\pm}$ obtained for ideal (*i.e.* non-dissipative) fluid dynamics are either purely real (outside the isentropic spinodal phase region where $v_s^2 > 0$) or purely imaginary (inside the isentropic spinodal region where $v_s^2 < 0$). Thus, in ideal fluid dynamics, the region of spinodal instability is bounded by the isentropic spinodal, $v_s(\rho, T) = 0$. The introduction of viscosity adds a negative imaginary amount to the frequency. We then have $\omega_{\boldsymbol{k}}^{\pm} \approx \mathring{\omega}_k - \frac{i}{2}\lambda_{\rm visc}k^2$ to first order in $\xi \equiv \frac{4}{3}\eta + \zeta$, where we have introduced the characteristic viscous length $\lambda_{\rm visc}(\rho, T) \equiv \xi(\rho, T)/h_0(\rho, T)c$. But the inclusion of viscosity does *not* change the region of instability. In contrast, the inclusion of heat conductivity expands the region of instability from the isentropic spinodal to the isothermal spinodal, $v_T(\rho, T) = 0$, and generally increases the spinodal growth rates.

For small distortions of uniform matter at given density and temperature, the dispersion relation yields the eigenfrequencies w_k in terms of the equation of state $p_T(\rho)$, the strength of the gradient term C, and the transport coefficients $\eta(\rho, T)$, $\zeta(\rho, T)$, and $\kappa(\rho, T)$. We describe below what we adopt for these key functions.

IV. TRANSPORT COEFFICIENTS

The deviation of the dynamical evolution from that of an ideal fluid is governed by three transport coefficients: the shear viscosity η and the bulk viscosity ζ (which here enter only through the effective viscosity $\xi \equiv \frac{4}{3}\eta + \zeta$) as well as the heat conductivity κ. Neither their magnitudes nor their dependencies on the environment (through ρ and T) are very well known. We shall therefore employ simple parametrizations of their functional form and introduce one adjustable overall strength parameter for each one, thus enabling us to conveniently explore a range of physical scenarios.

A. Viscosity

Using string theory methods, Kovtun *et al.* [15] made general arguments that the shear viscosity η, in any relativistic quantum field theory at finite temperature and zero chemical potential, has a lower bound, $\eta \geqslant \hbar\sigma/4\pi$, where σ is the associated entropy density. It might therefore seem natural to use $\eta = \eta_0\hbar\sigma/4\pi$, (i.e., simply scale the minimum value by the factor $\eta_0 \geqslant 1$). However, it has been argued [16] that values near the minimum should be expected only in the vicinity of the phase transformation. The use of a constant factor η_0 could therefore be regarded only as a rough approximation and a range of η_0 values should be explored.

The entropy density σ, while appropriate in the context of ultrarelativistic nuclear collisions where the medium has a high temperature and a very small net baryon density, is not suitable in the present context where the focus is on matter at high baryon density and relatively modest temperature [18]. A more appropriate quantity, suitable in both limits, is the enthalpy density $h(\rho, T) \equiv p + \varepsilon$ [18]. When the net baron density ρ vanishes it becomes $h = T\sigma$, whereas h/c^2 approaches the mass density at high baryon density and low temperature, $h \approx mc^2 n \gg T\sigma$, where n is density of particles and m is their mass. (For cold nuclear matter we have $n \approx \rho$, since the pions and antinucleons have negligible populations, and hence $m = m_N$.)

Furthermore, one would expect the viscosity to be proportional to the interparticle spacing $d \equiv 1/n^{1/3}$ [18], which provides a convenient measure of the mean free path in a dense fluid. When the plasma has no net baryon density, d is inversely proportional to the temperature T, $\hbar c/T = 4\pi c_0 d$. The conversion constant c_0 is given by

$$c_0 \;\equiv\; \frac{1}{4\pi}\left[\left(g_g + \frac{3}{2}g_q\right)\frac{\zeta(3)}{\pi^2}\right]^{\frac{1}{3}} \;\approx\; 0.12779. \tag{34}$$

Therefore, based on these considerations, we shall make the following ansatz,

$$\eta(\rho, T) \;\doteq\; \eta_0\frac{c_0}{c}\, d(\rho, T)\, h(\rho, T), \quad \eta_0 \geqslant 1, \tag{35}$$

which amounts to $\eta = \eta_0\hbar\sigma/4\pi$ in the baryon-free plasma, whereas it becomes $\eta \approx \eta_0 c_0 mcnd$ in the nonrelativistic gas. This latter expression is similar to the familiar expression from classical transport theory for the shear viscosity coefficient in

a dilute one-component gas, $\eta \approx \frac{1}{3} m \bar{v} n \ell$, where $\bar{v}$ is the mean particle speed and ℓ is its mean free path.

Because the bulk viscosity ζ is generally expected to be significantly smaller than the shear viscosity η, we shall take the effective viscosity to be $\xi \equiv \frac{4}{3}\eta + \zeta \approx \frac{4}{3}\eta$. It is convenient to introduce the associated characteristic length which is proportional to the interparticle spacing,

$$\lambda_{\rm visc}(\rho, T) \equiv \frac{1}{c} \frac{\xi(\rho, T)}{h(\rho, T)/c^2} = \frac{4}{3} \eta_0 \, c_0 \, d(\rho, T). \quad (36)$$

It should be noted, though, that the dependence of η and ζ on the environment may differ qualitatively. Thus it was found that the bulk viscosity associated with chiral restoration in baryon-free matter exhibits a singularity at the critical point [17]; it would obviously be valuable to extend that analysis to the scenario considered here: the confinement transformation in baryon-rich matter away from the critical point.

B. Heat conductivity

The thermal conductivity is fundamentally related to the viscosity because it derives from the same microscopic transport processes. In a dilute classical gas it can be expressed as $\kappa \approx \frac{1}{3} \bar{v} \ell c_v$, where $\bar{v}$ is the mean particle speed and $c_v \equiv \partial_T \varepsilon_T(\rho)$ is the heat capacity (equal to $\frac{3}{2} n$ for a dilute classical gas). Because $\bar{p} = m \bar{v}$ and $h \approx m c^2 n$, we see that $\kappa/\eta \approx c_v/(h/c^2)$. We therefore make the following ansatz,

$$\kappa(\rho, T) \doteq \kappa_0 \, c_0 \, c \, d(\rho, T) \, c_v(\rho, T), \quad \kappa_0 \geqslant 1, \quad (37)$$

with c_0 as given in Eq. (34) and assuming that the overall strength factor κ_0 should be at least unity. Although the relation $\kappa/\eta \approx c_v/(h/c^2)$ would suggest that the two normalization constants should be similar, $\kappa_0 \approx \eta_0$, we prefer to leave them separately adjustable to make it possible to explore the effects of the two distinct types of dissipation. The characteristic length scale associated with heat conduction is, then,

$$\lambda_{\rm heat}(\rho, T) \equiv \frac{1}{c} \frac{\kappa(\rho, T)}{c_v(\rho, T)} = \kappa_0 \, c_0 \, d(\rho, T). \quad (38)$$

Although the approximate expressions for the transport coefficients [Eqs. (35) and (37)] should not be expected to be accurate, they will serve well for our present purpose of exploring the effect of the dissipative mechanisms on the spinodal decomposition, because they enable us to easily control the overall dissipative effects.

C. Growth rates

The spinodal isothermal and isentropic boundaries determined by $v_T = 0$ and $v_s = 0$, respectively, pertain to the thermodynamic limit of very long wave lengths, $k \to 0$. When the wave number k is increased, the region of instability steadily shrinks as the gradient term gives an ever larger contribution to the pressure. Thus, at a given temperature T, the lower spinodal boundary density $\rho_A(k; T)$ increases steadily with k, while the upper spinodal boundary density $\rho_B(k; T)$ decreases steadily. For a fixed value of k, a contour plot of the growth rate γ_k in the (ρ, T) phase plane therefore exhibits a ridge between those two boundaries. The height of the ridge decreases steadily as T is increased, first rather gently due to the dominance of the fermions at low temperatures. The local value of the maximum wave number for which instabilities exist, $k_{\rm max}(\rho, T)$, will have a similar appearance.

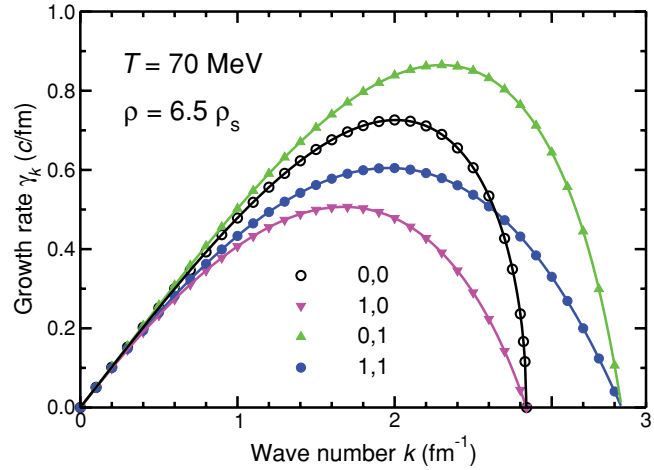

FIG. 2. (Color online) The growth rate $\gamma_k(\rho, T)$, as a function of the wave number k, calculated with finite-range fluid dynamics at $\rho = 6.5\,\rho_s$ and $T = 70\,$MeV for four different combinations of dissipation: no dissipation ($\eta_0 = 0, \kappa_0 = 0$); minimal viscosity but no heat conduction ($\eta_0 = 1, \kappa_0 = 0$); no viscosity but minimal heat conduction ($\eta_0 = 0, \kappa_0 = 1$); both minimal viscosity and minimal heat conduction ($\eta_0 = 1, \kappa_0 = 1$).

We now illustrate, in Fig. 2, the resulting dispersion relations for thermodynamic scenarios relevant to the present study. Selecting a phase point in the central region of the phase coexistence region where both the isothermal and the isentropic sound velocities are imaginary, $\rho = 6.5\rho_s$ and $T = 70\,$MeV (see Fig. 1), we consider the growth rate γ as a function of the wave number k of the density undulation being amplified. The nondissipative treatment with ideal finite-range fluid dynamics provides a convenient reference result. It yields a fastest growth time of about $t_0 \approx 1.38\,{\rm fm}/c$ which occurs for wave numbers near $k_0 \approx 2.0\,{\rm fm}^{-1}$, corresponding to an optimal wave length of $\ell_0 = 2\pi/k_0 \approx 3.14\,$fm.

Relative to this reference, the inclusion of viscosity slows the growth but does *not* change the domain of instability which is still delineated by the vanishing of the isentropic sound speed v_s. We see that the inclusion of a minimal amount of viscosity ($\eta_0 = 1$) leads to a significant reduction in γ and also shifts the optimal length scale toward larger values.

On the other hand, relative to the ideal scenario, the inclusion of heat conductivity enlarges the domain of instability, the boundary being now determined by the vanishing of the isothermal sound speed v_T. Thus, generally, the inclusion of heat conductivity increases the growth rates, particularly at the high end of the unstable k range.

While the inclusion of both minimal viscosity and minimal heat conduction necessarily enlarges the unstable k range, it does somewhat reduce the fastest growth rates. However, it hardly affects the scale of the fastest-growing modes, $k_{\rm max}$. As the strengths of the dissipative terms are further increased, the growth rate γ_k decreases steadily and, at the same time,

the maximum in the dispersion relation moves gradually downward in k.

These features are present throughout the unstable region of the (ρ, T) phase plane. To obtain an impression of how the growth rates change with ρ and T, we show in Fig. 3 the fastest growth rate γ_0 as we move away from the phase point explored in Fig. 2, either at constant T [Fig. 3(a)] or constant ρ [Fig. 3(b)], as indicated in Fig. 1. In these illustrations we show the ideal scenario where no dissipation is present $(\eta_0, \kappa_0 = 0)$, the scenario with minimal dissipation $(\eta_0, \kappa_0 = 1)$, and a scenario with five times stronger dissipation $(\eta_0, \kappa_0 = 5)$, thus covering the range suggested by the RHIC data [19–21]; the currently favored estimate is $\eta_0 \approx 1$–3. Because, as noted above, the heat conductivity is fundamentally related to the shear viscosity, it should be expected that their strengths vary in approximate unison; the effect of varying their relative strengths may be judged from the results shown in Fig. 2.

As expected from the discussion in the beginning of this section, the fastest growth at a given temperature occurs about midway between the corresponding spinodal boundaries. Furthermore, the temperature generally reduces the growth rates, though only weakly at small T. The curves in the Fig. 3(b) do not exhibit a monotonic decrease because the selected path along a constant density does not follow the ridgeline: the maxima in the curves shown in the top panel shift steadily toward smaller densities as T is increased, as would be expected from the general appearance of the phase diagram [see Fig. 1].

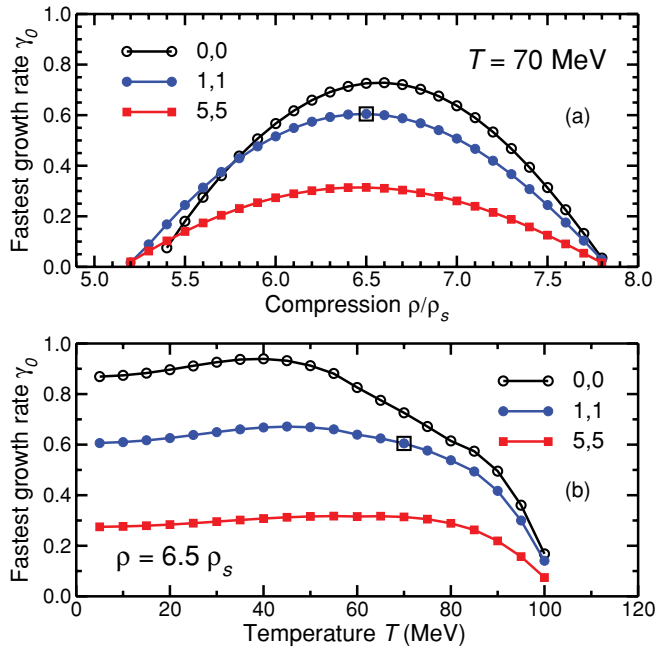

FIG. 3. (Color online) The maximum growth rate γ_0 (c/fm) shown at various compressions for fixed $T = 70\,\mathrm{MeV}$ (a) and at various temperatures for fixed compression $\rho/\rho_s = 6.5$ (b), for three different assumptions about the dissipation, namely no dissipation: $(\eta_0, \kappa_0) = (0, 0)$; minimal dissipation: (1, 1), and strong dissipation: (5, 5). The open square corresponds to the phase point at which the dispersion relation shown in Fig. 2 was obtained (using minimal dissipation).

Finally, we note that a fivefold increase in the dissipation above the minimal value, that is, changing (η_0, κ_0) from (1, 1) to (5, 5), leads to a reduction in the growth rates γ_k by only about a factor of two.

V. DYNAMICAL EVOLUTION

After the above preparations, we are now in a position to address the dynamical evolution of the unstable collective modes in the spinodal region of the phase diagram.

A. Dynamical phase trajectories

We first specify dynamical phase trajectories, $[\rho(t), T(t)]$, that are representative of the bulk matter in the collision zone, making use of the results presented in Ref. [22]. In that work, a number of different dynamical models were used to extract the time evolution of the net baryon density, $\rho(t)$, and the energy density, $\varepsilon(t)$, in the center of a head-on gold-gold collision for the range of collision energies anticipated at FAIR. The resulting dynamical trajectories in the (ρ, ε) phase plane were remarkably independent of the specific model, in large part probably because of the robust nature of the mechanical densities which are subject to conservation laws, in contrast to the corresponding thermodynamical variables (μ, T). Nevertheless, there were significant variations in the detailed behavior. This is illustrated in Fig. 4, which shows density evolutions $\rho(t)$ obtained with the three-fluid model [23] and ultrarelativistic quantum molecular dynamics (UrQMD) [24] at beam kinetic energies of 5 and 10 GeV/A. (Note that these beams are bombarded onto stationary targets, as will be done at FAIR; the same collision energies can be obtained in a collider configuration by using total beam energies of ≈1.8 and ≈2.4 GeV/A, respectively.) We utilize these results to construct the dynamical phase trajectories considered. [We emphasize that although we do consider the resulting trajectories as being plausible, we do not mean to

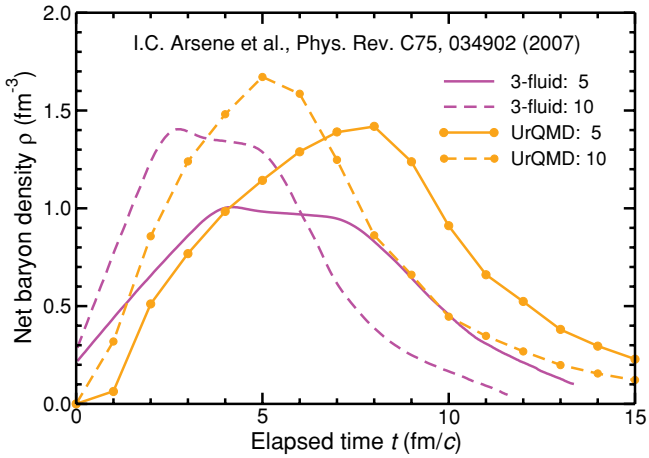

FIG. 4. (Color online) The time evolution of the net baryon density, $\rho(t)$, at the center of a head-on gold-gold collision for bombarding energies of 5 and 10 GeV/A, as calculated with the three-fluid [23] and the UrQMD [24] models (from Ref. [22]).

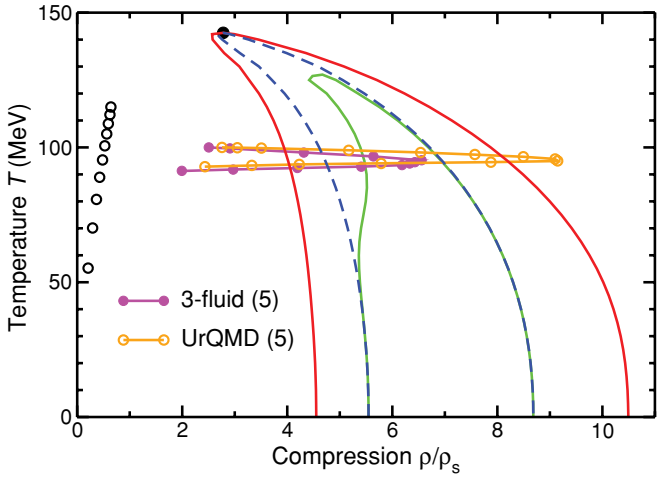

FIG. 5. (Color online) Dynamical phase trajectories based on the three-fluid and UrQMD density evolutions (shown in Fig. 4) obtained for 5 GeV/A in Ref. [22]; the associated time-dependent growth rates $\gamma_{\boldsymbol{k}}(t)$ are illustrated in Fig. 6. The symbols along the trajectories are equidistant in time with $\Delta t = 1\,\mathrm{fm}/c$, whereas the open dots on the left indicate the freezeout locations for bombarding energies of $E = 1, \ldots, 10\,\mathrm{GeV}/A$ obtained from fits to experimental data as discussed in Ref. [25].

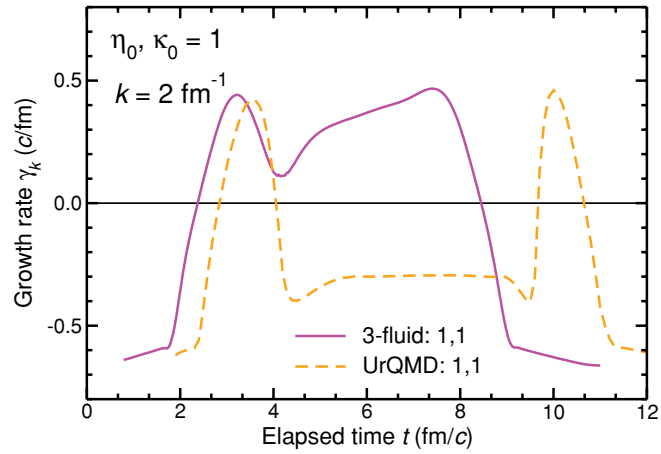

FIG. 6. (Color online) The spinodal growth rate $\gamma_{\boldsymbol{k}}(t) = \mathrm{Re}[\omega_{\boldsymbol{k}}(t)]$ for modes with $k = 2\,\mathrm{fm}^{-1}$, calculated with minimal dissipation along the two dynamical (ρ, T) phase trajectories shown in Fig. 5.

endorse either one of these specific models. Indeed, essentially identical evolutions could have been generated by a number of existing models by suitable tuning of the bombarding energy. In particular, a trajectory very similar to the one based on calculations with the three-fluid model at 5 GeV/A could likely have been obtained with the UrQMD model at a somewhat lower collision energy (but such calculations are not presently available).]

As expected, the degree of amplification achieved depends strongly on the length of time spent in the phase region of spinodal instability. To elucidate this key feature, we consider in some detail the phase trajectories depicted in Fig. 5. The density evolutions $\rho(t)$ are those calculated with the two models for 5GeV/A, while the temperature evolutions $T(t)$ are (somewhat arbitrarily) prescribed with an eye toward the freeze-out conditions extracted from data [25]. The essential difference between these two trajectories is that UrQMD yields compressions that reach all the way into the deconfined phase region, whereas the maximum compression achieved with the three-fluid model lies inside the unstable region. Such a situation would be obtained with UrQMD as well at a somewhat lower collision energy (3–4 GeV/A).

When the turning point of the phase trajectory lies inside the unstable region, the modes are exposed to the spinodal amplification for a longer time and, consequently, the resulting degree of amplification will be maximized. This key fact is illustrated in Fig. 6. For the penetrating (UrQMD) trajectory, the modes are exposed to amplification only during the two relatively brief periods when the phase point is traversing the spinodal region (and the amplification gained during the compressional traverse is largely lost during the high-density stage due to the equilibration process so only the amplification received during the expansion traverse is relevant). By contrast, the more optimal (three-fluid) trajectory provides amplification for a sustained period of time, thus making a phase separation more likely to occur.

Although it is yet difficult to make specific predictions about the optimal collision energy, it seems evident that such an energy range exists, because the location of the (ρ, T) phase point associated with the maximum compression (the turning point) moves steadily downward as the collision energy is lowered. The experimentally known freeze-out temperatures (indicated on the left in Fig. 5) provide a lower bound on the phase region that could be accessed by nuclear collisions. The turning point is therefore likely to traverse the unstable phase region at fairly high temperatures where it is relatively narrow. Consequently, the optimal range of collision energy is most likely not so wide. Because of this generic expectation, we shall take the above phase trajectories as being reasonably representative of what may happen in the bulk region of an actual collision.

B. Dissipative collective dynamics

As the bulk of the evolving system traverses the unstable phase region, its density fluctuations may be amplified. To make quantitative estimates of this effect, we employ the method developed in Ref. [26] for the evolution of collective modes subject to a dissipative coupling to the environment [i.e., to the (many more) noncollective modes in the system].

The treatment considers an ensemble of $\mathcal{N}$ macroscopically similar systems $\{n\}$ that have all been prepared with the same average density ρ_0 relative to which individual perturbations are introduced,

$$\rho^{(n)}(\boldsymbol{r}) \;=\; \rho_0 + \delta\rho^{(n)}(\boldsymbol{r}) \;=\; \rho_0 + \sum_{\boldsymbol{k}\neq 0} \rho_{\boldsymbol{k}}^{(n)} \mathrm{e}^{i\boldsymbol{k}\cdot\boldsymbol{r}}. \qquad (39)$$

Generally, such as during the expansion stage of a nuclear collision, the bulk density is time dependent. We shall assume that the effect of this overall evolution may be taken into account approximately by using the corresponding

time-dependent transport coefficients in the formulas below. We should then think of the mode index $\boldsymbol{k}$ as a mode number $\boldsymbol{K}$ rather than a wave number, because the expansion primarily stretches the modes without introducing much mode mixing [27]. In this way we may obtain the spatial size of the resulting fluctuations by scaling the initial wave length with the linear expansion factor, $[\rho_0(t_i)/\rho_0(t_f)]^{D/3}$, where D is the effective dimensionality of the expansion.

The primary object of study is the associated spatial correlation function, $\sigma(\boldsymbol{r}_{12}) = \prec \delta\rho(\boldsymbol{r}_1)\,\delta\rho(\boldsymbol{r}_2)^* \succ$, where

$$\prec \delta\rho(\boldsymbol{r}_1)\,\delta\rho(\boldsymbol{r}_2)^* \succ \equiv \frac{1}{\mathcal{N}} \sum_n \delta\rho^{(n)}(\boldsymbol{r}_1)\,\delta\rho^{(n)}(\boldsymbol{r}_2)^* \qquad (40)$$

is the ensemble average and $\boldsymbol{r}_{12} \equiv \boldsymbol{r}_1 - \boldsymbol{r}_2$. The Fourier transform of $\sigma(\boldsymbol{r})$ provides a convenient measure of the degree of density fluctuation at a given scale because it is the ensemble average of $|\rho_{\boldsymbol{k}}|^2$,

$$\sigma_{\boldsymbol{k}}^2 = \prec |\rho_{\boldsymbol{k}}|^2 \succ = \int \frac{d\boldsymbol{r}}{V}\, \mathrm{e}^{-i\boldsymbol{k}\cdot\boldsymbol{r}} \sigma(\boldsymbol{r}). \qquad (41)$$

We are generally interested in the evolution of the collective modes in the system. Adopting the treatment of Ref. [26], we assume that the amplitude $\rho_{\boldsymbol{k}}$ of a given collective mode $\boldsymbol{k}$ is governed by an equation of motion having the form,

$$\frac{d}{dt}\rho_{\boldsymbol{k}}(t) = -i\,\omega_{\boldsymbol{k}}(t)\rho_{\boldsymbol{k}}(t) + B_{\boldsymbol{k}}(t). \qquad (42)$$

The complex eigenfrequencies $\omega_{\boldsymbol{k}} = \epsilon_{\boldsymbol{k}} + i\,\gamma_{\boldsymbol{k}}$ are determined by the dispersion equation derived above, while the Brownian term $B_{\boldsymbol{k}}$ describes the residual coupling between the collective mode and the reservoir (i.e., the noncollective modes of the system). It is fluctuating in nature and is assumed to be Markovian,

$$\prec B_{\boldsymbol{k}}(t)\, B_{\boldsymbol{k}'}(t')^* \succ = 2\mathcal{D}_{\boldsymbol{k}\boldsymbol{k}'}(t)\,\delta(t-t'). \qquad (43)$$

The equal-time correlation coefficient for two collective modes, $\sigma_{\boldsymbol{k}\boldsymbol{k}'}(t) \equiv \prec \rho_{\boldsymbol{k}}(t)\rho_{\boldsymbol{k}'}(t)^* \succ$, is then given by [26],

$$\sigma_{\boldsymbol{k}\boldsymbol{k}'}(t) = \sigma_{\boldsymbol{k}\boldsymbol{k}'}(t_i)\, e^{-i\omega_{\boldsymbol{k}\boldsymbol{k}'}t} + 2\int_{t_i}^{t} dt'\, \mathcal{D}_{\boldsymbol{k}\boldsymbol{k}'}(t')\, e^{i\omega_{\boldsymbol{k}\boldsymbol{k}'}(t'-t)}, \qquad (44)$$

if $\omega_{\boldsymbol{k}\boldsymbol{k}'} \equiv \omega_{\boldsymbol{k}} - \omega_{\boldsymbol{k}'}^*$ is constant. It is readily seen that it satisfies the following differential equation,

$$\frac{d}{dt}\sigma_{\boldsymbol{k}\boldsymbol{k}'}(t) = -i\,\omega_{\boldsymbol{k}\boldsymbol{k}'}(t)\sigma_{\boldsymbol{k}\boldsymbol{k}'}(t) + 2\mathcal{D}_{\boldsymbol{k}\boldsymbol{k}'}(t), \qquad (45)$$

which was dubbed the "Lalime equation" in Ref. [26].

For our present studies, we are particularly interested in the time evolution of the diagonal components of the covariance matrix, $\sigma_{\boldsymbol{k}\boldsymbol{k}} = \sigma_{\boldsymbol{k}}^2$, which are equal to the fluctuation coefficients introduced in Eq. (41). Then

$$\sigma_{\boldsymbol{k}}^2(t) = \left[\sigma_{\boldsymbol{k}}^2(t_i) + \int_{t_i}^{t} 2\mathcal{D}_{\boldsymbol{k}}(t')\, e^{-2\Gamma_{\boldsymbol{k}}(t')} dt'\right] e^{2\Gamma_{\boldsymbol{k}}(t)}, \qquad (46)$$

where $\mathcal{D}_{\boldsymbol{k}} \equiv \mathcal{D}_{\boldsymbol{k}\boldsymbol{k}}$ and we have introduced the following *amplification coefficient*,

$$\Gamma_{\boldsymbol{k}}(t) \equiv \int_{t_i}^{t} \mathrm{Im}[\omega_{\boldsymbol{k}}(t')]\, dt' = \int_{t_i}^{t} \gamma_{\boldsymbol{k}}(t')\, dt'. \qquad (47)$$

If the environment is stationary, then $\gamma_{\boldsymbol{k}}$ and $\mathcal{D}_{\boldsymbol{k}}$ remain constant in time, so $\Gamma_{\boldsymbol{k}}(t) = \gamma_{\boldsymbol{k}}(t - t_i)$, and we obtain a simple exponential time evolution,

$$\sigma_{\boldsymbol{k}}^2(t) = \frac{\mathcal{D}_{\boldsymbol{k}}}{\gamma_{\boldsymbol{k}}}[e^{2\gamma k(t-t_i)} - 1] + \sigma_{\boldsymbol{k}}^2(t_i)\, e^{2\gamma k(t-t_i)}. \qquad (48)$$

When $\gamma_{\boldsymbol{k}}$ is negative, as is normally the case, the mode is stable and relaxes exponentially toward its equilibrium value $\tilde{\sigma}_{\boldsymbol{k}}^2$, $\sigma_{\boldsymbol{k}}^2(t) \to -\mathcal{D}_{\boldsymbol{k}}/\gamma_{\boldsymbol{k}}$, the associated relaxation time being $t_{\boldsymbol{k}} = 1/\gamma_{\boldsymbol{k}}$. More generally, within the stable regime, $\sigma_{\boldsymbol{k}}^2(t)$ will seek to relax toward its instantaneous equilibrium value $\tilde{\sigma}_{\boldsymbol{k}}^2(t) = -\mathcal{D}_{\boldsymbol{k}}(t)/\gamma_{\boldsymbol{k}}(t)$, in accordance with the Einstein relation. In the opposite case, when $\gamma_{\boldsymbol{k}}$ is positive, the mode is unstable and the fluctuations exhibit an exponential growth, with both the original mode fluctuations $\sigma_{\boldsymbol{k}}^2(t_i)$ and the noise $\mathcal{D}_{\boldsymbol{k}}/\gamma_{\boldsymbol{k}}$ being amplified.

The diffusion coefficients $\mathcal{D}_{\boldsymbol{k}}$ represent the coupling of the collective modes to the residual system. They thus play two important roles in the dynamical evolution of the density fluctuations. In the stable regime (as mentioned above) the coupling determines the relaxation times $t_{\boldsymbol{k}}$ for the relaxation of the fluctuation coefficients $\sigma_{\boldsymbol{k}}^2$ toward their appropriate equilibrium values $\tilde{\sigma}_{\boldsymbol{k}}^2$, whereas in the unstable regime it continually produces additional fluctuations that are also amplified. Thus, even in the absence of initial fluctuations, the coupling of the collective mode to the residual system will continually create fluctuations that will subsequently become amplified or damped, as governed by the Lalime equation (45). In particular, the diffusion coefficients enable the stable modes to continually adjust their fluctuations as the equilibrium variances evolve.

C. Onset of phase separation

The amplification coefficient $\Gamma_{\boldsymbol{k}}$ defined in Eq. (47) is obtained by integrating $\gamma_{\boldsymbol{k}} \equiv \mathrm{Im}(\omega_{\boldsymbol{k}})$ over the entire time interval considered. When there is no dissipation, $\omega_{\boldsymbol{k}}^2$ is always real so $\gamma_{\boldsymbol{k}}$ vanishes outside the unstable region. But in the presence of dissipation, $\gamma_{\boldsymbol{k}}$ is negative outside the unstable region, and increasingly so the stronger the dissipation. As a result, the local relaxation time is reduced, which in turn ensures that the fluctuations remain close to their equilibrium value until shortly before the trajectory enters the unstable region. However, by the same token, any amplification acquired while the trajectory is inside the unstable region is correspondingly quickly lost after the trajectory has reentered the normal region and again equilibrates. In fact, the dissipative length tends to be larger at late times, due to the increased particle spacing in the more dilute system, thus shortening the relaxation time.

Our present study aims to clarify the prospects for the spinodal amplification to become sufficiently large to cause a phase-separating clumping of the system. Because our treatment is perturbative, it is only valid as long as the fluctuations remain relatively small. The occurrence of large fluctuations in the calculation should then be taken as a signal that clumping is likely. It should be recalled that the bulk of the system is thermodynamically unstable so even a modest degree of fluctuation may cause a catastrophic breakup. The prospects

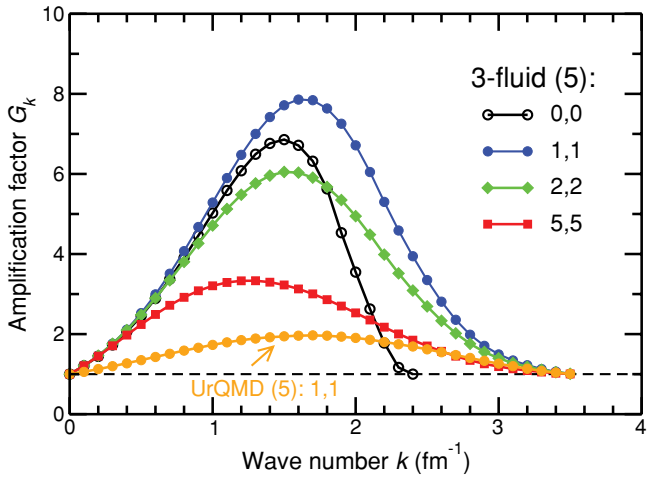

FIG. 7. (Color online) As a function of the wave number k is shown the amplification factor G_k [see Eq. (49)] resulting from motion along the three-fluid phase trajectory displayed in Fig. 5 for various degrees of dissipation (indicated by the values of η_0 and κ_0). Also shown is the result for the UrQMD trajectory in Fig. 5 using minimal dissipation [i.e., $(\eta_0, \kappa_0) = (1, 1)$].

for this to occur are enhanced by the fact that fluctuations created in the mechanically unstable (spinodal) region may become further amplified during the traverse of the adjacent metastable region, just as impurities introduced in this region may trigger condensation.

Thus, the key question is how much amplification may occur during the unstable era. To elucidate this issue in a quantitative manner, we extract the following *amplification factor*,

$$G_{\boldsymbol{k}} \equiv \exp\left(\int_{>} \gamma_{\boldsymbol{k}}(t)\,dt\right), \tag{49}$$

where the integral is only over those times during which the mode is unstable, $\gamma_{\boldsymbol{k}} > 0$.

Figure 7 shows values of G_k obtained for the entire range of wave numbers, as obtained with various degrees of dissipation. Although we concentrate on the phase trajectory that reaches its maximum compression inside the spinodal region (the one based on the three-fluid model results for 5 GeV/A), we also show the result of a more penetrating trajectory to bring out the importance of tuning the collision energy for optimal effect.

In addition to the result of ideal fluid dynamics, we show results for various degrees of dissipation, ranging from minimal [i.e., $(\eta_0, \kappa_0) = (1, 1)$] to five times that. Although viscosity generally slows the evolution, thus also suppressing the growth of instabilities, heat conductivity generally increases the growth rate. The combined effect of introducing small amounts of dissipation then tends to enhance the amplification. Thus, the resulting degree of nonuniformity is fairly robust against moderate changes in the dissipation strength and, consequently, our conclusions do not appear to be sensitive to the specific parametrizations of the transport coefficients.

The results displayed in Fig. 7 bring out the characteristic feature of spinodal instability, namely that the amplification mechanism favors certain length scales. We note that the two-point correlation coefficient σ_k^2 is proportional to G_k^2 and thus exhibits a stronger peaking. More generally, because the N-point correlation is proportional to G_k^N, the spinodal effect manifests itself progressively stronger in the higher-order correlations.

We see that G_k is peaked around $k_0 \approx 1.6$–$1.3\,\mathrm{fm}^{-1}$, depending on the degree of dissipation, which corresponds to wave lengths $\ell_0 = 2\pi/k_0 \approx 3.9$–$4.8$ fm. If, at a temperature of 80–100 MeV, a uniform system situated at the lower edge of the spinodal region (hence having a density $\rho_0 \approx 5\rho_s$) transforms itself into plasma drops embedded in a hadron gas, with each subsystem having the corresponding coexistence density, $\rho_1(T) \approx 4\rho_s$ and $\rho_2(T) \approx 8\rho_s$, then we may expect the drop radius to be $R_{\mathrm{drop}} \approx \frac{1}{2}\ell_0[(\rho_0 - \rho_1)/(\rho_2 - \rho_0)]^{1/3} \approx$ 1.2–1.5 fm. Each such drop would then have a baryon number of 10–18. Since this is only a relatively small fraction of the collision system one would expect that several such drops would be formed during the phase separation. On the other hand, a drop of such a size is sufficiently large to be regarded as a macroscopic source that will undergo statistical hadronization.

VI. CONCLUDING REMARKS

In the exploration of the phase diagram of strongly interacting matter by means of nuclear collisions, the mechanism of spinodal phase decomposition might give rise to unique signals of the first-order phase transition. For the planning of possible experimental campaigns to search for spinodal phase separation, it is useful to have estimates of which bombarding energies are expected to be optimal for producing the effect. The analysis presented above suggests that these bombarding energies lie at the lower end of the anticipated FAIR range. It is also well within the energy region proposed for NICA but appears to be too low for experiments at RHIC to be feasible.

However, when making a quantitative prediction of the optimal collision energy range, it should be kept in mind that the calculated dynamical phase trajectories [22], on the basis of which we made our estimates, extracted the conditions right at the center of the collision zone. Therefore, they most likely provide an upper limit on the compression and it must be expected that the average compression and excitation over an extended volume will be smaller than those shown in Figs. 4 and 5. Consequently, the optimal bombarding energy is probably somewhat higher than what the above idealized analysis would suggest. For example, it may well be that the 5 GeV/A UrQMD simulation, whose maximum compression overshoots the spinodal region, would be quite suitable for spinodal clumping because the average degree of compression over an extended region favors phase separation.

It should also be recognized that the spinodal phase region is surrounded by a thermodynamically metastable region through which the phase trajectory has to pass after the spinodal mechanism has acted. During this traverse, sufficiently significant deviations from uniformity will be further amplified and phase separation is thus more likely to occur than suggested by just the perturbative treatment employed here. In fact, the spinodal amplification of the preexisting fluctuations may be

regarded as merely providing seeds for a subsequent nonlinear breakup evolution in the metastable region. (For a study of the nucleation mechanism, see Ref. [11].)

We note the analogy with the search for spinodal fragmentation [5] as a signal of the nuclear liquid-gas phase transition [6]. The collision energy had to be carefully adjusted to producing the phenomenon: a too-high energy would yield an explosive vaporization, whereas a too-low energy would cause the two nuclei to fuse (and subsequently deexcite by light-particle emission). But in the optimal energy range, the bulk of the combined system would first compress (to 2–3 times normal) and then start to expand; however, the expansion would tend to stall, leaving the system in a dilute (and nearly spherical) configuration for a sufficient length of time (several times the typical growth time) to cause the most unstable modes to grow dominant, thereby leading the system toward a breakup into nearly equal-sized intermediate-mass fragments. Our present analysis suggests that collisions at suitably tuned relativistic energies would also cause the bulk of the system to spend several growth times inside the unstable phase region and thus enable the spinodal formation of plasma drops.

In the liquid-gas case the production of equal-size nuclear fragments in each event provided a simple and unambiguous signal of the spinodal breakup mechanism and thus for the existence of a first-order transition. The confinement transition is inherently more difficult to investigate experimentally because any plasma drops that may have been formed will ultimately hadronize and are thus harder to identify. Nevertheless, the transient existence of such spatially separated blobs of deconfined matter may be revealed by careful examination of suitable multiparticle correlations. Although some relatively schematic studies have already been made for the purpose of identifying such observables [28–30] there is a need for much more refined studies. We hope that the present investigation, which suggests that spinodal phase separation might indeed occur, will provide an incentive for such endeavors.

ACKNOWLEDGMENTS

We acknowledge helpful discussions with V. Koch, J. Liao, H. C. Song, and D. N. Voskresensky. This work was supported by the Director, Office of Energy Research, Office of High Energy and Nuclear Physics, Nuclear Physics Division of the US Department of Energy under Contract No. DE-AC02-05CH11231.

APPENDIX A: EQUATION OF STATE

The present study requires an equation of state of strongly interacting matter that displays the expected phase structure. Although significant progress has been made in understanding the thermodynamical properties of each of the phases separately, our current understanding of the phase coexistence region is not yet on firm ground. We therefore employ a conceptually simple approximate equation of state that will suffice for our present explorations.

For this purpose, we approximate the confined phase by an ideal gas of nucleons and pions augmented by a density-dependent interaction energy, while the deconfined phase is taken as an ideal gas of quarks and gluons with their interactions described by a bag constant. The desired phase structure is then generated by suitable interpolation between these two pure phases.

1. Confined phase

The confined phase is approximated as an ideal gas of pions, nucleons, and antinucleons, plus an interaction term. The total hadronic pressure is, thus,

$$p^H = p_\pi + p_N + p_{\bar{N}} + p_w, \tag{A1}$$

where the contribution from the ideal pion gas is

$$p_\pi(T) = -g_\pi T \int_{m_\pi}^{\infty} \frac{p\epsilon d\epsilon}{2\pi^2} \ln[1 - e^{-\beta\epsilon}], \tag{A2}$$

with $g_\pi = 3$ and $m_\pi = 140\,\mathrm{MeV}$, while the nucleons and antinucleons contribute

$$p_N(T, \mu_0) = g_N \int_{m_N}^{\infty} \frac{p\epsilon d\epsilon}{2\pi^2} \ln[1 + e^{-\beta(\epsilon-\mu_0)}], \tag{A3}$$

$$p_{\bar{N}}(T, \mu_0) = g_N \int_{m_N}^{\infty} \frac{p\epsilon d\epsilon}{2\pi^2} \ln[1 + e^{-\beta(\epsilon+\mu_0)}], \tag{A4}$$

respectively, with $g_N = 2 \times 2 = 4$ and $m_N = 940\,\mathrm{MeV}$. The net baryon density $\rho^H = \rho_N - \rho_{\bar{N}}$ then follows,

$$\rho^H = \frac{\partial p^H}{\partial \mu_0} = g_N \int_{m_N}^{\infty} \frac{p\epsilon d\epsilon}{2\pi^2} \frac{\sinh \beta\mu_0}{\cosh \beta\mu_0 + \cosh \beta\epsilon}, \tag{A5}$$

and the entropy density is $\sigma^H = \partial p^H / \partial T$. Finally, the contribution from the interaction energy density $w(\rho)$ is $p_w(\rho) = \rho\partial_\rho w(\rho) - w(\rho)$ and the parameter μ_0 is related to the chemical potential μ by $\mu = \mu_0 + \partial_\rho w$.

The interaction energy density $w(\rho)$ has the form,

$$w(\rho) = \left[-A \left(\frac{\rho}{\rho_s} \right)^\alpha + B \left(\frac{\rho}{\rho_s} \right)^\beta \right] \rho, \tag{A6}$$

where we use $\alpha = 1$ and $\beta = 2$. The strength coefficients A and B are then adjusted so that nuclear matter saturates at $\rho_s = 0.153\,\mathrm{fm}^{-3}$ and the associated compression modulus is $K \equiv 9(\rho^2 \partial_\rho^2 e_0(\rho))_s = K_N + K_w = 300\,\mathrm{MeV}$, where $K_N = -\frac{6}{5} E_F \approx -43\,\mathrm{MeV}$ is the contribution from the Fermi motion of the nucleons (which is *negative*). The binding energy of nuclear matter is then also roughly reproduced. The resulting equation of state for nuclear matter is shown in Fig. 8.

2. Deconfined phase

The deconfined phase is taken as an ideal gas of massless gluons and light quarks with a standard bag constant,

$$p^Q = p_g + p_q + p_{\bar{q}} - B, \tag{A7}$$

where $p_g = g_g(\pi^2/90)T^4$ with $g_g = 2 \times 8 = 16$ is the gluon pressure while the quarks and antiquarks contribute

$$p_q + p_{\bar{q}} = g_q \left[\frac{7\pi^2}{360} T^4 + \frac{1}{12} \mu_q^2 T^2 + \frac{1}{24\pi^2} \mu_q^4 \right], \tag{A8}$$

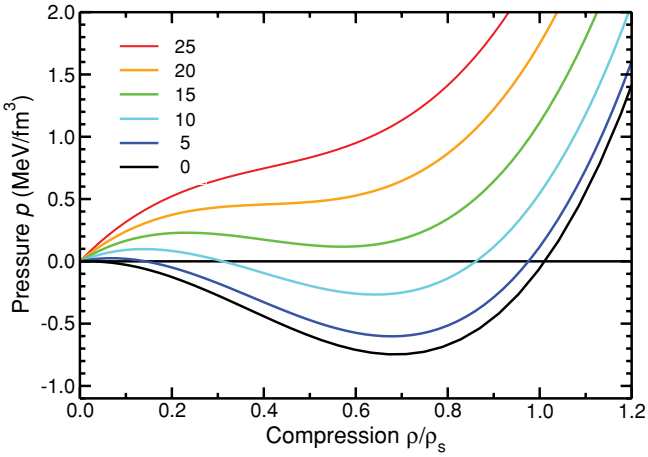

FIG. 8. (Color online) The equation of state, $p_T(\rho)$, for the (ρ, T) region relevant for ordinary nuclear matter: the dependence of the pressure on the compression for specified T (shown in MeV).

with $g_q = 2 \times 3 \times 2 = 12$ and $\mu_q = \frac{1}{3}\mu$. The net baryon density in the plasma is then

$$\rho^Q = \frac{\partial p^Q}{\partial \mu} = \frac{2}{9}\mu T^2 + \frac{2}{81\pi^2}\mu^3, \tag{A9}$$

while the entropy density is

$$\sigma^Q = \frac{\partial p^Q}{\partial T} = \frac{74}{45}\pi^2 T^3 + \frac{2}{9}\mu^2 T. \tag{A10}$$

For the bag constant we use $B = 300\,\mathrm{MeV/fm^3}$.

3. Interpolation

At zero temperature and zero chemical potential, the pressure of the nucleon gas vanishes whereas that of the quark gas is equal to $-B$. The confined phase is then the thermodynamically favored one. However, as the chemical potential is raised, the plasma pressure increases faster than the hadronic pressure, so the two curves, $p^H(T = 0, \mu)$ and $p^Q(T = 0, \mu)$, cross at a certain value of μ, above which the deconfined phase is favored, as illustrated in Fig. 9. This phase crossing procedure can be repeated for any temperature up to $T_{\max}$ and the resulting crossing points are included in Fig. 9. The corresponding coexistence densities are shown in Fig. 10.

For the discussion of phase coexistence, it is convenient to work in the canonical representation where the temperature is specified. Then, the condition of phase coexistence (i.e., same temperature, chemical potential, and pressure at two different densities ρ_1 and ρ_2) amounts to the condition that $f_T(\rho)$, the free-energy density as a function of density, have common tangents. This is readily seen because $\mu_T(\rho) = \partial_\rho f_T(\rho)$ implies that the two chemical potentials are then equal, $\mu_1 = \mu_2$, and because the tangent at ρ_i is given by $t_i(\rho) = f_i(\rho) + (\rho - \rho_i) f_i'(\rho)$ the fact that $t_1(\rho) = t_2(\rho)$ immediately implies $p_1 = p_2$.

Figure 11 shows $f^H_{T=0}(\rho)$ and $f^Q_{T=0}(\rho)$. The former curve starts at zero but grows more rapidly than the latter, which starts at B, so the two curves cross and, furthermore, because they both have positive curvature, a common tangent exists.

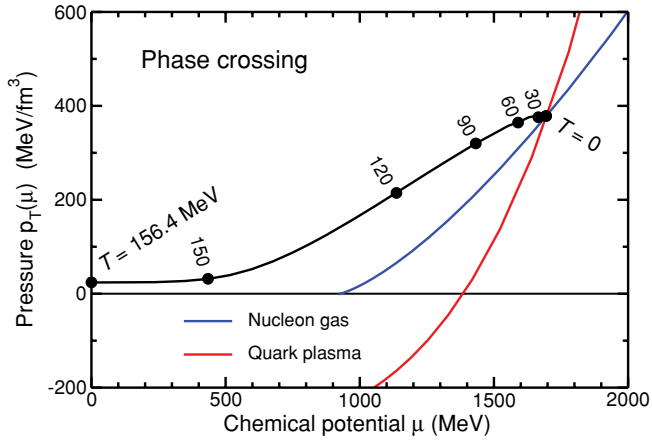

FIG. 9. (Color online) Phase crossing: The pressures in the two idealized phases are shown as functions of the chemical potential μ for $T = 0$; the systems are in mutual thermodynamic equilibrium at the μ value for which the two curves cross. The crossing points obtained by the same procedure for $T > 0$ are connected by the solid curve, which terminates at $T_{\max} \approx 156.4\,\mathrm{MeV}$.

Because of this generic feature, it is expected that cold matter exhibits a first-order phase transition when compressed.

Although the simple gas models employed presumably provide reasonable (though still somewhat idealized) descriptions of the two individual phases well away from the coexistence region, neither one is suitable in the phase-coexistence region. To describe the transition region, we represent the free-energy density there by a fifth-order polynomial $\tilde{f}_T(\rho)$ that matches the values of f_T^H, $\partial_\rho f_T^H$, and $\partial_\rho^2 f_T^H$ at a density $\tilde{\rho}_T^H \lesssim \rho_T^H$ and the values of f_T^Q, $\partial_\rho f_T^Q$, and $\partial_\rho^2 f_T^Q$ at a density $\tilde{\rho}_T^Q \gtrsim \rho_T^Q$, where ρ_T^H and ρ_T^Q are those densities at which the two idealized curves $f_T^H(\rho)$ and $f_T^Q(\rho)$ have a common tangent. For lower densities, $\rho \leqslant \tilde{\rho}_T^H$, we use the idealized hadron gas, $f_T^H(\rho)$, and at higher energies, $\rho \geqslant \tilde{\rho}_T^Q$, we use the idealized plasma, $f_T^Q(\rho)$.

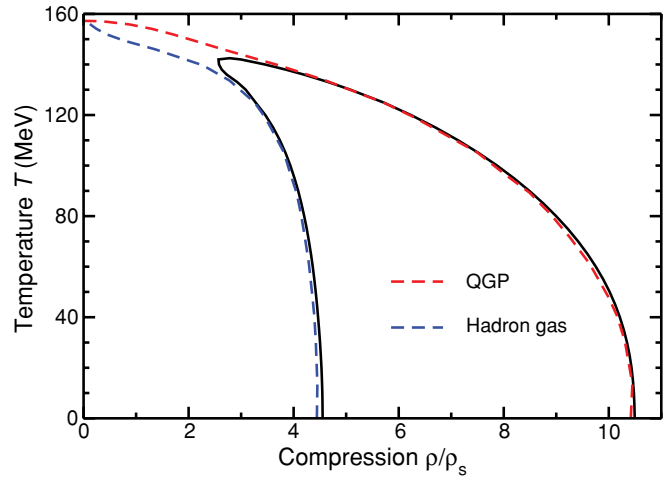

FIG. 10. (Color online) Phase crossing: For the range of temperatures where the two idealized phases coexists, $0 \leqslant T \leqslant T_{\max} \approx 156.4$ MeV, the associated coexistence densities are shown (dashed curves). The solid curves show the corresponding coexistence densities for the spline-based equation of state.

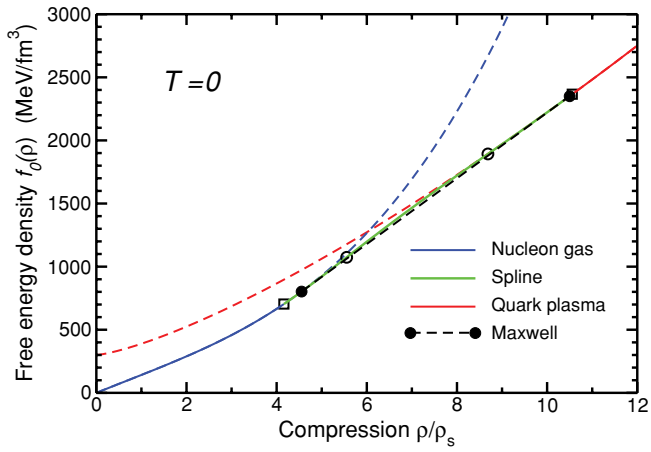

FIG. 11. (Color online) The free-energy density at zero temperature, $f_{T=0}(\rho)$, as a function of the degree of compression ρ/ρ_c. The two individual phases $f_0^H(\rho)$ and $f_0^Q(\rho)$ are shown together with the connection between them, $\tilde{f}_0(\rho)$, obtained by splining between the two open squares located at $\tilde{\rho}_0^H$ and $\tilde{\rho}_0^Q$. The resulting coexistence points (solid circles) are located at ρ_1 and ρ_2; they are connected by the associated common tangent (the Maxwell line). The spinodal boundary densities ρ_A and ρ_B are indicated by the open circles.

When the lower matching density $\tilde{\rho}_T^H$ is chosen sufficiently close to ρ_T^H and the higher matching density $\tilde{\rho}_T^Q$ is chosen sufficiently close to ρ_T^Q then the resulting spline function $\tilde{f}_T(\rho)$ also has a common tangent and so the system has a first-order transition at the particular temperature T. The associated densities [where the common tangent touches $\tilde{f}_T(\rho)$] are then the coexistence densities, ρ_1 and ρ_2, at that temperature.

This spline procedure is illustrated in Fig. 11 for $T = 0$ and the corresponding pressure is shown in Fig. 12. By suitable adjustment of the matching densities $\tilde{\rho}_T^H$ and $\tilde{\rho}_T^Q$, it is thus possible to design an equation of state having the desired phase structure, namely a first-order phase transition that becomes ever weaker as the temperature is raised and terminates in a critical point at a finite density ρ_c. The resulting phase coexistence boundaries, (ρ_1, T) and (ρ_2, T), are shown in Fig. 10, the full phase diagram having already been shown in Fig. 1.

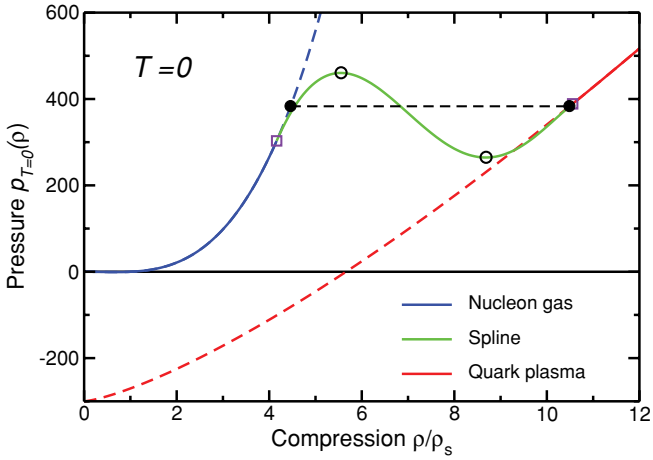

FIG. 12. (Color online) The pressure at zero temperature, $p_{T=0}(\rho)$, as a function of the degree of compression ρ/ρ_c, corresponding to the free-energy density shown in Fig. 11. The two individual phases are shown together with the connection between them obtained by splining between the two open squares. The resulting coexistence points (open circles) are connected by the associated Maxwell line. The spinodal boundaries are situated at the two extrema (open circles).

APPENDIX B: SPLINE METHOD

We describe here a convenient spline method that enables us to match values and derivatives at two points.

We seek a polynomial expression for the function $f(x)$ [here the free-energy density $f_T(\rho)$] that matches the specified values $a_0 \equiv f(x = a)$ and $b_0 \equiv f(x = b)$ as well as the associated derivatives up to any order n, $a_i \equiv f_a^{(i)} \equiv (d^i f/dx^i)_{x=a}$ and $b_i \equiv f_b^{(i)} \equiv (d^i f/dx^i)_{x=b}$, $i = 1, \ldots, n$.

If $f_{n-1}(x)$ denotes the spline approximation that matches derivatives up to the $(n-1)^{\text{th}}$ order (which is a polynomial of order $2n-1$), then we may obtain the approximation for the next order n by writing

$$f_n(x) = f_{n-1}(x) + (b-x)^n(x-a)^n \frac{(b-x)\alpha_n + (x-a)\beta_n}{b-a}. \tag{B1}$$

Because the factor $(b-x)^n(x-a)^n$ and its derivatives up to order $n-1$ vanish at a and b, it follows that $f_n(x)$ satisfies the matching conditions up to order $n-1$ [i.e., $f_n^{(i)}(a) = f_{n-1}^{(i)}(a) = a_i$ and $f_n^{(i)}(b) = f_{n-1}^{(i)}(b) = b_i$ for $i < n$].

The only remaining task is thus to determine the two coefficients α_n and β_n which can be done by matching also the n^{th} derivative at a and b, namely $f_a^{(n)} \doteq a_n$ and $f_b^{(n)} \doteq b_n$. It is elementary to show that they are given by the following expressions,

$$\alpha_n = \frac{a_n - f_{n-1}^{(n)}(a)}{n!(b-a)^n}, \quad \beta_n = \frac{b_n - f_{n-1}^{(n)}(b)}{n!(a-b)^n}. \tag{B2}$$

It is possible to also determine the derivatives of the spline function by iteration. In particular, the derivatives at the two matching points are given by

$$f_\nu^{(n)}(a) = f_{\nu-1}^{(n)}(a) + \frac{n!\,\nu!(-)^{n-\nu}}{(n-\nu)!\,(2\nu-n+1)!} \times [(\nu+1)\alpha_\nu - (n-\nu)\beta_\nu], \tag{B3}$$

$$f_\nu^{(n)}(b) = f_{\nu-1}^{(n)}(b) + \frac{n!\,\nu!(-)^{\nu}}{(n-\nu)!\,(2\nu-n+1)!} \times [(\nu+1)\beta_\nu - (n-\nu)\alpha_\nu], \tag{B4}$$

where the first terms are present only for $n < 2\nu$, whereas the second terms are present only for $\nu \leqslant n \leqslant 2\nu + 1$. We note that

$$f_n^{(2n+1)}(a) = (2n+1)!(-)^n[\beta_n - \alpha_n] = f_n^{(2n+1)}(b), \tag{B5}$$

consistent with the fact that the highest nonzero derivative is a constant.

The above expressions can be used iteratively to determine the spline polynomial $f_n(x)$ for any order $n \geqslant 0$ as well as all of its $2n+1$ derivatives.

[1] B. I. Abelev *et al.*, Internal STAR Note SN0493, 2009: [drupal.star.bnl.gov/STAR/starnotes/public/sn0493].
[2] B. Friman, C. Höhne, J. Knoll, S. Leupold, J. Randrup, R. Rapp, and P. Senger, *The CBM Physics Book* (Springer, Berlin, 2010, in press).
[3] A. N. Sissakian and A. S. Sorin, J. Phys. G **36**, 064069 (2009).
[4] R. A. L. Jones, *Soft Condensed Matter* (Oxford University Press, Oxford, 2002).
[5] Ph. Chomaz, M. Colonna, and J. Randrup, Phys. Rep. **389**, 263 (2004).
[6] B. Borderie *et al.*, Phys. Rev. Lett. **86**, 3252 (2001).
[7] J. Randrup, Phys. Rev. C **79**, 054911 (2009).
[8] V. V. Skokov and D. N. Voskresensky, Nucl. Phys. A **828**, 401 (2009).
[9] L. P. Csernai and I. N. Mishustin, Phys. Rev. Lett. **74**, 5005 (1995).
[10] J. Randrup, Phys. Rev. Lett. **77**, 1226 (1996).
[11] L. P. Csernai and J. I. Kapusta, Phys. Rev. D **46**, 1379 (1992).
[12] A. Muronga, Phys. Rev. C **76**, 014909 (2007).
[13] H. Heiselberg, C. J. Pethick, and D. G. Ravenhall, Ann. Phys. **223**, 37 (1993).
[14] J. Randrup, Phys. Rev. Lett. **92**, 122301 (2004).
[15] P. K. Kovtun, D. T. Son, and A. O. Starinets, Phys. Rev. Lett. **94**, 111601 (2005).
[16] L. P. Csernai, J. I. Kapusta, and L. D. McLerran, Phys. Rev. Lett. **97**, 152303 (2006).
[17] K. Paech and S. Pratt, Phys. Rev. C **74**, 014901 (2006).
[18] J. Liao and V. Koch, Phys. Rev. C **81**, 014902 (2010).
[19] U. Heinz, in *Relativistic Heavy Ion Physics*, edited by R. Stock, Landolt-Börnstein: Numerical Data and Functional Relationships in Science and Technology—New Series, Vol. I/23 (Springer Verlag, Heidelberg, 2010), Sec. 5.1.
[20] D. A. Teaney, Rep. Prog. Phys. **72**, 126001 (2009).
[21] H. C. Song and U. Heinz, J. Phys. G **36**, 064033 (2009).
[22] I. C. Arsene, L. V. Bravina, W. Cassing, Yu. B. Ivanov, A. Larionov, J. Randrup, V. N. Russkikh, V. D. Toneev, G. Zeeb, and D. Zschiesche, Phys. Rev. C **75**, 034902 (2007).
[23] Yu. B. Ivanov, V. N. Russkikh, and V. D. Toneev, Phys. Rev. C **73**, 044904 (2006).
[24] S. A. Bass, Prog. Part. Nucl. Phys. **41**, 255 (1998); M. Bleicher *et al.*, J. Phys. G **25**, 1859 (1999).
[25] J. Randrup and J. Cleymans, Phys. Rev. C **74**, 047901 (2006).
[26] M. Colonna, Ph. Chomaz, and J. Randrup, Nucl. Phys. A **567**, 637 (1994).
[27] M. Colonna, Ph. Chomaz, A. Guarnera, and B. Jacquot, Phys. Rev. C **51**, 2671 (1995).
[28] D. Bower and S. Gavin, Phys. Rev. C **64**, 051902 (2001).
[29] J. Randrup, Acta Phys. Hung. **22**, 69 (2005).
[30] V. Koch, A. Majumder, and J. Randrup, Phys. Rev. C **72**, 064903 (2005).